

1 **Sequential formation and resolution of multiple rosettes drives embryo remodeling after**  
2 **implantation**

3

4

5 Neophytos Christodoulou<sup>1,4</sup>, Christos Kyprianou<sup>1,4</sup>, Antonia Weberling<sup>1</sup>, Ran Wang<sup>2</sup>,  
6 Guizhong Cui<sup>2</sup>, Guangdum Peng<sup>2</sup>, Naihe Jing<sup>2,3</sup> and Magdalena Zernicka-Goetz<sup>1\*</sup>

7

8

9 **Affiliations:**

10 <sup>1</sup> Mammalian Embryo and Stem Cell Group, University of Cambridge, Department of  
11 Physiology, Development and Neuroscience; Downing Street, Cambridge, CB2 3DY, UK

12 <sup>2</sup> State Key Laboratory of Cell Biology, CAS Center for Excellence in Molecular Cell  
13 Science, Shanghai Institute of Biochemistry and Cell Biology, Chinese Academy of Sciences;  
14 University of Chinese Academy of Sciences, 320 Yue Yang Road, Shanghai 200031, China

15 <sup>3</sup> School of Life Science and Technology, ShanghaiTech University, 100 Haike Road,  
16 Shanghai 201210, China

17

18 <sup>4</sup> equal contribution

19 \*corresponding author: mz205@cam.ac.uk

20

21 **Summary**

22 **The dramatic morphogenetic remodeling of embryo architecture after implantation**  
23 **culminates in pro-amniotic cavity formation. Despite its key importance, how this**  
24 **transformation occurs remains unknown. Here, we apply high-resolution imaging of**  
25 **embryos developing *in vivo* and *in vitro*, spatial RNA sequencing and 3D trophoblast-**  
26 **stem-cell models to determine the sequence and mechanisms of these remodeling events.**  
27 **We show that cavitation of the embryonic tissue is followed by folding of extra-**  
28 **embryonic tissue to mediate formation of a second, extra-embryonic cavity.**  
29 **Concomitantly, at the boundary between embryonic and extra-embryonic tissues, a**  
30 **hybrid 3D rosette forms. Resolution of this rosette enables the embryonic cavity to**  
31 **invade the extra-embryonic tissue. Subsequently,  $\beta$ 1-integrin signalling mediates**  
32 **formation of multiple extra-embryonic 3D rosettes. Podocalyxin exocytosis leads to their**  
33 **polarized resolution permitting extension of embryonic and extra-embryonic cavities**  
34 **and their fusion into a unified pro-amniotic cavity. These morphogenetic**  
35 **transformations of embryogenesis bring a novel mechanism for lumen expansion and**  
36 **fusion.**

37

38 **Keywords:** mammalian embryo, post-implantation morphogenesis, 3D rosette, lumen  
39 formation

40

## 41 **Introduction**

42 Embryogenesis involves a gradual increase in complexity of embryo architecture as cells and  
43 tissues take shape. These events require intricate coordination and in mammals involve close  
44 cooperation between embryonic and extra-embryonic tissues that become established by the  
45 time of implantation<sup>1-4</sup>. The embryonic tissue, the epiblast, will give rise to the new organism,  
46 while one of the two extra-embryonic tissues, the trophoctoderm, will generate the extra-  
47 embryonic ectoderm giving rise to the placenta and the other, the primitive endoderm, will  
48 generate the visceral endoderm and finally the yolk sac. The critical interaction between these  
49 tissues during mouse implantation development enables the transformation of the blastocyst  
50 into the egg cylinder, a more complex structure with an entirely different architecture.

51 The major morphogenetic event in the blastocyst-to-egg cylinder transition involves  
52 formation of the pro-amniotic cavity that spans the whole length of the egg cylinder. We have  
53 shown that this morphogenesis is initiated by polarization and lumenogenesis of the  
54 embryonic compartment that is triggered by  $\beta 1$ -integrin signalling<sup>5,6</sup> and coordinated with a  
55 transition in stem cell potential<sup>5,6</sup>. However, how the lumen becomes established in the  
56 trophoctoderm-derived extra-embryonic compartment and how then the embryonic and extra-  
57 embryonic lumens unify to form single cavity have remained unknown. Here, we use mouse  
58 embryos developing *in vivo* and *in vitro* together with 3D stem cell models, high resolution  
59 time-lapse microscopy and spatio-temporal transcriptome analyses to determine the sequence  
60 of events and mechanisms underlying coordination between the embryonic and extra-  
61 embryonic tissues in driving embryo remodeling and pro-amniotic cavity formation.

## 62 **Results**

### 63 **Morphogenetic steps of pro-amniotic cavity formation**

64 To understand how the pro-amniotic cavity forms, we first sought to determine the sequence  
65 of morphogenetic events involved. Based on detailed observations of 142 embryos freshly  
66 recovered during implantation stages, we could distinguish five distinct stages of global  
67 tissue rearrangements culminating in pro-amniotic cavity formation (Fig. 1a-e). During stage  
68 I (E4.75-5.0 embryos), epiblast cells became polarized into a rosette-like structure with a  
69 lumen opening at its centre, as previously described<sup>5</sup>, while trophoctoderm cells proliferated  
70 with the most proximal cells undergoing apical constriction. In stage II (E5.25-5.5 embryos),  
71 a thin elongated cavity formed at the proximal end of the extra-embryonic ectoderm as a  
72 result of tissue folding (Fig. 1f-h; Fig. S1, Movie 1-3). During stage III (E5.5 embryos), the

73 epiblast rosette re-organized into a cup-shaped epithelium while extra-embryonic ectoderm  
74 cells at the embryonic/extra-embryonic boundary became polarized with their apical sides  
75 flanking the epiblast cavity. At the same time, the apico-basal polarity axis of the epiblast at  
76 the embryonic/extra-embryonic boundary changed from parallel to perpendicular, relative to  
77 the proximo-distal axis of the embryo (Fig. 1b,e). During stage IV (E5.5-E5.75 embryos), the  
78 embryonic cavity extended into the extra-embryonic compartment (Fig. 1b). Finally, during  
79 stage V (E5.75 embryos), the two cavities fused into a unified single cavity spanning the  
80 whole embryo. These observations allowed us to determine the sequence of cellular re-  
81 organization that remodels the embryonic and extra-embryonic tissues leading to pro-  
82 amniotic cavity formation.

### 83 **Extra-cellular matrix is required for morphogenesis of extra-embryonic compartment**

84 As extra-cellular matrix (ECM) signalling directs the formation of a cellular rosette that  
85 undergoes lumenogenesis in the embryonic compartment<sup>5</sup>, we wondered whether a similar  
86 mechanism operates in the extra-embryonic compartment. High resolution analysis of tissue  
87 remodeling on the cellular level revealed that immediately upon implantation, the extra-  
88 embryonic compartment is comprised of two cell populations: one on the outside in direct  
89 contact with the basement membrane (BM), and a second on the inside (n=35 embryos, Fig.  
90 2a). While the outside cells were apico-basally polarized, as revealed by the distribution of  
91 Golgi apparatus and cell shape, the inside cells were not (Fig. 2a-c). Since laminin is a ligand  
92 for integrin receptors<sup>7</sup>, we hypothesized that such a polarization mechanism could act via the  
93 ECM surrounding the extra-embryonic compartment. Analysis of the activation status of  $\beta$ 1-  
94 integrin, the main ECM signalling mediator<sup>8</sup> on the basal side of the outside extra-embryonic  
95 cells (Fig. S2a), supported this hypothesis.

96 To determine whether the ECM is sufficient to provide the signalling cues required for  
97 polarization of the extra-embryonic ectoderm, we established a trophoblast stem cell (TSC)  
98 3D model to mimic the development of the extra-embryonic compartment *in vitro*. This  
99 entailed the suspension of small clumps of TSCs in 3D Matrigel (as ECM substitute). We  
100 found that provision of ECM components led TSCs to arrange into spherical aggregates  
101 resembling the extra-embryonic compartment (n=20, Fig. 2d). Whereas the TSCs in contact  
102 with the ECM acquired columnar polarized morphology, TSCs not in contact with the ECM  
103 retained an apolar character (Fig. 2d-e), supporting a role for the ECM in the polarization of

104 extra-embryonic cells. TSCs clumps cultured in the absence of the ECM failed to polarize  
105 confirming that the ECM is necessary for TSCs polarization (Fig. S2b).

106 To determine whether provision of the ECM is indeed required for polarization of extra-  
107 embryonic ectoderm *in vivo*, we disrupted the ECM by treating embryos with collagenase IV  
108 (COLIV)<sup>9</sup>. The COLIV treatment led to BM disruption and defective  $\beta$ 1-integrin activation  
109 (Fig. S2c-d): whereas outside cells in control embryos polarized, the outside cells of COLIV-  
110 treated embryos did not (n=12 and 13 respectively; Fig. 2f-g; Fig. S2e). These results indicate  
111 that ECM-mediated signalling is necessary for extra-embryonic ectoderm organization.

### 112 **ECM/ $\beta$ 1-integrin signalling is required for extra-embryonic compartment cavitation**

113 As  $\beta$ 1-integrin signalling plays a central role in cell polarization in many different systems  
114 <sup>5,10</sup>, we therefore hypothesized that it might be required for polarization of the extra-  
115 embryonic compartment. Since  $\beta$ 1-integrin knock-out embryos die during the implantation  
116 period<sup>11</sup>, we tested our hypothesis using the TSC 3D system and a  $\beta$ 1-integrin blocking  
117 antibody<sup>12</sup>. TSCs cultured in the presence of the  $\beta$ 1-integrin blocking antibody became  
118 disorganized and apolar, in contrast to the organized and polarized control aggregates (n=20  
119 for each group, Fig. 2h-j; Fig. S2f). Therefore, blocking  $\beta$ 1-integrin function caused failure of  
120 TSC polarization that resembled the effects of ECM disruption and loss of  $\beta$ 1-integrin  
121 activity upon extra-embryonic ectoderm polarization.

122 Since the above results indicated that extra-embryonic ectoderm polarizes in response to an  
123 ECM/ $\beta$ 1-integrin-dependent mechanism, we next assessed whether ECM/ $\beta$ 1-integrin-  
124 mediated polarization is essential for pro-amniotic cavity morphogenesis. To this end we  
125 recovered embryos just after implantation and cultured them for 24 hrs in the absence or  
126 presence of COLIV. Whereas in the great majority of cultured control embryos the  
127 embryonic and extra-embryonic cavities fused, this process failed in most COLIV-treated  
128 embryos (Fig. 2k-l). Importantly, COLIV-treated embryos in which the formation of the pro-  
129 amniotic cavity was unaffected (3/27 embryos) had a residual BM (Fig. 2k right panel).  
130 These results indicate that ECM/ $\beta$ 1-integrin-mediated polarization of the extra-embryonic  
131 ectoderm is essential for pro-amniotic cavity morphogenesis.

### 132 **ECM/ $\beta$ 1-integrin signalling drives the formation of extra-embryonic rosettes**

133 To determine the cellular dynamics as the extra-embryonic compartment forms, we analyzed  
134 82 freshly collected embryos prior to the fusion of the cavities. We found that in contrast to

135 the embryonic compartment, the extra-embryonic compartment of nearly all E5.5 embryos  
136 examined (93%, n=82) had multiple rosette structures (Fig. 3a; Fig. S3a). These extra-  
137 embryonic rosettes comprised 6 to 10 cells (n=60 rosettes, 40 E5.5 embryos) and had all the  
138 features of epithelial rosettes described thus far<sup>13,14</sup>: the apical localization of polarity markers  
139 (aPKC, Par6, ZO-1) and actomyosin, indicated that extra-embryonic ectoderm cells were  
140 apically polarized towards the rosette's centre (Fig. 3b). Strikingly, the number of extra-  
141 embryonic rosettes depended on the developmental stage: they were present more frequently  
142 in stages II and III; their frequency was significantly reduced in stage IV and were  
143 completely absent in stage V (so after cavities fusion) (Fig. 3c).

144 The majority of epithelial rosettes described so far are 2D structures forming within single-  
145 layered epithelia<sup>15</sup>. 3D cell segmentation analyses revealed that extra-embryonic rosettes are  
146 3D structures (Fig. 3d-e; Movie 4). However, in contrast to other 3D rosettes that participate  
147 in lumen formation<sup>5,16</sup>, the extra-embryonic rosettes do not form lumens (n=60 rosettes, 40  
148 E5.5 embryos) and, unusually, two adjacent rosettes could share cells that are bipolar  
149 contributing to both a rosette and the cavity (Fig. 3d-f; Movie 5).

150 To gain insight into the role of rosettes during extra-embryonic morphogenesis, we examined  
151 their formation. Analyses of 142 embryos revealed that as many as 95% of the rosettes only  
152 contacted the BM on one side (with their outer cells) and had a second group of inner cells  
153 that, although polarized with their apical side towards the rosette's centre, were not in contact  
154 with the BM (Fig. S3b-d). This led us to hypothesize that inner cell polarization might be  
155 dependent upon outer cells becoming polarized through ECM/ $\beta$ 1-integrin signalling. To test  
156 this hypothesis, we analyzed the organization of rosettes in COLIV-treated embryos in which  
157 polarization of outside cells was prevented. In contrast to all control embryos, rosette  
158 formation was defective in the presence of COLIV (n=12 and n=12 control and experimental  
159 embryos respectively) (Fig. 3g-h). Together, these results suggest that ECM- $\beta$ 1-integrin  
160 signalling is required for polarization of outside cells as well as subsequent polarization of  
161 inside cells and rosette formation (Fig. 3i).

## 162 **Resolution of extra-embryonic rosettes drives pro-amniotic cavity formation**

163 The defective pro-amniotic cavity formation seen in the absence of extra-embryonic rosettes  
164 suggested an involvement of these rosettes in cavity formation. To address this possibility,  
165 we analyzed the timing of events leading to the appearance of rosettes in relation to the five  
166 stages of pro-amniotic cavity formation we observed here (Fig. 1a-b). We found that just

167 before the re-organization of the epiblast from a sphere to a cup-shaped epithelium, a rosette  
168 consisting of embryonic and extra-embryonic cells was established at the boundary between  
169 the compartments (Fig. 4a). The formation of this hybrid rosette was preceded by the  
170 breakdown of the BM separating the two compartments at stage I (E4.75; n=20 embryos, Fig.  
171 4b). Importantly, resolution of this hybrid rosette was concomitant with epiblast remodeling  
172 from a sphere to a cup-shaped epithelium (E5.5, n=10 embryos, Fig. 4c).

173 To establish the exact sequence of these events, we filmed the development of embryos  
174 expressing LifeAct-GFP transgene<sup>17</sup>. This revealed a strong apical enrichment of actin at the  
175 centre of the hybrid rosette. This actin enrichment was lost just before resolution of the  
176 hybrid rosette, allowing the cavity to progress into the extra-embryonic compartment (Fig.  
177 4d; Fig. S4, Movie 6,7). We confirmed that epiblast cells contributing to a hybrid rosette re-  
178 oriented their polarity so that a tract of cells with common polarization connected the centre  
179 of the rosette with the cavity (Fig. 4e). To determine if loss of cell-cell adhesion along this  
180 track drives cavity extension, we laser ablated epiblast cells at the adhesion sites connecting  
181 the epiblast cavity with the centre of the hybrid rosette. This laser ablation led to hybrid  
182 rosette resolution and cavity progression (Fig. 4f; Movie 8), confirming that loss of adhesion  
183 at specific sites of epiblast cells drives the cavity progression.

184 After hybrid rosette resolution, a new rosette became established near the embryonic/extra-  
185 embryonic boundary in proximity to the expanding embryonic cavity (Fig. 4d). This rosette  
186 comprised only extra-embryonic cells and was detected only in stage II and III embryos  
187 (n=20 embryos; Fig. S5a). The main morphological change during the transition from stage  
188 III to IV was the extension of the embryonic cavity. We found that at stage III, embryos  
189 typically displayed a tract of the polarized apical parts of cells extending from the tip of the  
190 embryonic cavity to the centre of an adjacent extra-embryonic rosette (Fig. 5a; Movie 9).  
191 When embryos reached stage IV, extra-embryonic cells facing the embryonic cavity acquired  
192 an open rosette conformation (Fig. 5b; Fig. S5b), suggesting that resolution of the rosettes  
193 drives the extension of the cavity during the transition from stage III to IV.

194 To visualize the dynamics of cavity extension, we filmed the development of embryos  
195 expressing membrane-Tomato<sup>18</sup> or LifeAct-GFP. This revealed that the resolution of a rosette  
196 near the embryonic/extra-embryonic boundary preceded the extension of the epiblast cavity  
197 (Fig. 5c; Fig. S5c; Movie 10-11). Specifically, rosette cells lost adhesion at cell interfaces  
198 connecting the epiblast cavity with the centre of the rosette (blue and purple cells Fig. 5c,

199 magenta and cyan cells Fig. S5c) in agreement with our observations of embryos developing  
200 *in vivo*.

201 Finally, we found that the centres of rosettes appearing near the extra-embryonic cavity were  
202 linked with the tip of the extra-embryonic cavity through polarized tracts, priming the  
203 cavity's expansion during stage IV (Fig. 5d; Fig. S5d-e; Movie 12). These observations  
204 suggest that progressive expansion of embryonic and extra-embryonic cavities upon  
205 resolution of rosettes results in their fusion (Fig. S5f, Movie13). Together, the observations of  
206 tissue remodeling of embryos developing *in vivo* and *in vitro* indicate that rosettes play a  
207 central role in pro-amniotic cavity formation.

### 208 **Polarized Podocalyxin exocytosis during rosette resolution and cavities expansion**

209 To gain insight into the molecular mechanisms of polarized rosette resolution and fusion of  
210 cavities, we generated a spatial transcriptome map<sup>19</sup> of post-implantation embryos by  
211 generating sequential sections of embryos along their proximo-distal axis at successive  
212 developmental stages and performing RNA sequencing (Fig. 6a; Table S1). These analyses  
213 revealed three distinct cell populations corresponding to distal visceral endoderm, epiblast  
214 and extra-embryonic ectoderm. The identity of these tissues was confirmed by examining the  
215 spatial expression pattern of epiblast (*Pou5f1*) and extra-embryonic ectoderm (*Cdx2*) markers  
216 (Fig. S6a-b). Additionally, *Wnt3* transcripts were detected in the distal extra-embryonic  
217 ectoderm and proximal epiblast and *T/Brachyury* transcripts were detected in the distal extra-  
218 embryonic ectoderm of E5.75 embryos (Fig. S6c) as described previously<sup>20</sup>, highlighting the  
219 sensitivity of this method.

220 Analysis of differential gene expression between embryonic and extra-embryonic regions  
221 revealed the upregulation of 764 genes in the E5.25 embryo extra-embryonic compartment;  
222 1119 genes in the E5.5 embryo extra-embryonic compartment; and 306 genes in the E5.75  
223 embryo extra-embryonic compartment (Table S1, Fig.S7a). Importantly, functional  
224 enrichment analysis revealed that several genes involved in integrin-mediated signalling were  
225 specifically upregulated in the extra-embryonic compartment during stages II-III (Fig. S6d,  
226 Table S1). This is in accord with our results showing that ECM/integrin signalling drives  
227 extra-embryonic tissue polarization and rosette formation.

228 In accord with the requirement for Rab11-mediated exocytosis and the reorganization of  
229 exocytotic vesicles in lumen formation<sup>6,21-23</sup>, we found several regulators of exocytosis and  
230 vesicle organization to be upregulated in the extra-embryonic compartment during pro-



231 amniotic cavity formation (Fig. 6b, Table S1). Specifically, expression of Rab11A, the main  
232 mediator of exocytosis during lumen formation, was enriched in the extra-embryonic  
233 compartment, suggesting that Rab11-mediated apical exocytosis is involved in this process.

234 In MDCK cells, lumenogenesis requires Par/aPKC mediated cell polarization and the  
235 concerted activity of Rab GTPases, to direct the polarized exocytosis of Podocalyxin<sup>16</sup>.  
236 Examination of expression dynamics of genes involved in the regulation of Podocalyxin  
237 exocytosis revealed that they were upregulated in the extra-embryonic compartment either at  
238 one or both stages of tissue remodeling (II, E5.25 or III E5.5), during which time the  
239 transcriptional profile of the extra-embryonic lineage differs from stage IV-V(E5.75) (Fig.6c;  
240 Fig.7a; Fig.S7b). Together this suggests that Podocalyxin exocytosis plays a role during pro-  
241 amniotic cavity formation.

242 In agreement with the transcriptome analysis, we found Podocalyxin positive exocytotic  
243 vesicles in all cells of the extra-embryonic compartment at E5.5, whereas in the embryonic  
244 compartment Podocalyxin was present only at the apical side of cells (Fig.7b). These  
245 Podocalyxin vesicles showed a polarized pattern of secretion, along the borders of polarized  
246 tracts connecting rosettes with cavities, in both hybrid and extra-embryonic rosettes (Fig. 7c-  
247 d). After fusion of the cavities, the extra-embryonic ectoderm cells not contributing to the  
248 cavity still contained Podocalyxin exocytotic vesicles (Fig.7e). Polarized cell intercalation  
249 resulted in the formation of a pseudostratified epithelium in the extra-embryonic  
250 compartment in which all the extra-embryonic ectoderm cells faced the cavity (Fig.8a,  
251 Fig.S8, Movie 14). At this point all the cells facing the cavity were negative for exocytotic  
252 vesicles (Fig.8b). These results indicate that whereas polarized rosette resolution drives the  
253 initial fusion of cavities, further tissue remodeling driven by intercalation completes the  
254 process during the final step of pro-amniotic cavity formation.

255

## 256 **Discussion**

257 Upon implantation, the blastocyst transforms into the egg cylinder, a structure of an entirely  
258 different architecture. We show that this drastic remodeling is driven by a series of major  
259 morphogenetic events that we break down into five stages: stage I) polarization and  
260 lumenogenesis of the embryonic tissue and generation of the extra-embryonic tissue; stage II)  
261 the folding of the extra-embryonic tissue leading to its lumenogenesis and formation of a  
262 hybrid rosette on the embryonic/extra-embryonic boundary; stage III) remodeling of the

263 embryonic tissue and formation of multiple 3D rosettes within the extra-embryonic tissue  
264 mediated by ECM- $\beta$ 1-integrin signalling; stage IV) the polarized resolution of extra-  
265 embryonic rosettes mediating expansion of embryonic and extra-embryonic cavities mediated  
266 by Rab11/Podocalyxin vesicles exocytosis; stage V) the fusion of embryonic and extra-  
267 embryonic cavities and polarized cell intercalation resulting in the formation of a unified pro-  
268 amniotic cavity (Fig. 8c).

269 Two-dimensional rosettes have been described to contribute to tissue re-arrangements during  
270 morphogenesis in many model systems<sup>15</sup>. Three-dimensional rosettes on the other hand, were  
271 shown to contribute to tissue shaping by generating self-contained central lumens rather than  
272 by rearranging cells<sup>5,16</sup>. Our detailed analysis of embryos developing *in vivo* as well as time-  
273 lapse imaging of embryos developing *in vitro* indicate that whereas extra-embryonic  
274 ectoderm rosettes have the characteristics of 3D epithelial rosettes, they do not form self-  
275 contained lumens but, instead, form and resolve in a polarized manner to permit extension of  
276 cavities through the compact extra-embryonic tissue. The spatial and temporal profile of  
277 morphogenetic reorganization accords with progressive resolution of rosettes from the  
278 embryonic to the extra-embryonic lumen to form the pro-amniotic cavity.

279 Our results indicate that resolution of extra-embryonic ectoderm rosettes is preceded by re-  
280 orientation of cell polarity and expansion of the apical domain in a subset of cells. This  
281 creates polarized tracts along cell interfaces connecting lumens with the centers of rosettes.  
282 This re-orientation of cell polarity is followed by polarized exocytosis and lumen extension,  
283 as Rab11/Podocalyxin vesicles become targeted to the rosettes' polarized tracts. Podocalyxin  
284 is a negatively charged sialomucin causing membrane repulsion<sup>24</sup> and therefore its secretion  
285 at these sites could indeed result in rosette resolution. Since we observe that each rosette is  
286 exposed to the cavity before its resolution, it is possible that osmotic pressure from the cavity  
287 fluid contributes to membrane separation during rosette resolution. Thus, a model proposing  
288 that rosette resolution driven by exocytosis mediates expansion of the cavities is more in line  
289 with our data than mechanisms described for lumen expansion in other systems<sup>25,26</sup>.

290 In summary, the detailed developmental, cellular and molecular characterization of the  
291 morphogenetic steps involved in the reorganization of the blastocyst into the egg cylinder  
292 structure leads us to propose a novel mechanism for cavity fusion that is mediated by tissue  
293 rearrangements governed by the formation and polarized resolution of multiple multicellular  
294 3D rosettes. Our model suggests that polarized resolution of these cell arrangements mediates

295 the remodeling of the whole embryo leading to fusion of embryonic and extra-embryonic  
296 cavities. Reorientation of apico-basal polarity, cell rearrangement and the expansion and  
297 fusion of cavities have been described during development of different organisms<sup>27-30</sup> and  
298 therefore it is likely that the morphogenetic processes leading to cavity formation we describe  
299 here might represent a common molecular and cellular mechanism utilized in processes other  
300 than mammalian embryogenesis.

301

### 302 **Author Contributions**

303 N.C and C.K designed and carried out the experiments and data analysis. A.W contributed to  
304 embryo live imaging. G.C and G.P performed the embryo cryosection, laser microdissection  
305 and library construction experiments for RNA-seq. R.W carried out the RNA sequencing  
306 analysis. N.J supervised the work related to spatial transcriptome analysis. M.Z.G conceived,  
307 supervised the study and wrote the manuscript with the help of N.C and C.K.

308

### 309 **Acknowledgments**

310 We are grateful to D. Glover, F. Antonica, M. Shahbazi, G. Amadei and S. Harrison for  
311 feedback on the manuscript. J. Nichols for the Confetti TSCs, I. Roswell (Francis Crick  
312 Institute) for LifeAct-GFP mice and Kevin O'Holleran (Cambridge Advanced Imaging  
313 Center, CAIC) for help with laser ablation experiments. The M.Z.G lab is supported by grants  
314 from the European Research Council (669198) and the Wellcome Trust (098287/Z/12/Z) and  
315 the EU Horizon 2020 Marie Skłodowska-Curie actions (ImageInLife,721537). C.K is  
316 supported by BBSRC Doctoral training studentship.

317

### 318 **Methods**

319 **Embryo recovery and culture:** Mice were kept in the animal house in accordance with  
320 national and international guidelines. All experiments have been regulated by the Animals  
321 (Scientific Procedures) Act 1986 Amendment Regulations 2012 following ethical review  
322 by the University of Cambridge Animal Welfare and Ethical Review Body (AWERB).  
323 Experiments were approved by the Home Office (Licence number: 70/8864). Animals  
324 were inspected daily and those that showed health concerns were culled by cervical  
325 dislocation. Implantation stage embryos were recovered from wild type F1, MF1 or CD1  
326 females mated with mTmG<sup>18</sup>, LifeAct-GFP<sup>17</sup> and wild type males. Pre-implantation embryos

327 were flushed out from the uteri as previously<sup>5</sup>. Post-implantation embryos were dissected out  
328 of the deciduae and transferred into IVC2<sup>31</sup>. After recovery, the embryos were transferred  
329 into drops of IVC2 (1 embryo/drop) covered with mineral oil and cultured according to the  
330 experimental designed. For the enzymatic removal of the BM, Collagenase IV (500ug/ml)  
331 was used for 3-5 hrs in IVC2 and then replaced with 50ug/ml for overnight culture. Embryos  
332 were cultured at 37°C in 5% CO<sub>2</sub>.

333 **Immunostaining:** Embryos were fixed in 4% paraformaldehyde (PFA) for 20 min at room  
334 temperature. Post-implantation embryos were permeabilized for ~12-20 min in 0.3% Triton  
335 X-100 / 0.1M Glycin in PBS. The primary antibodies were then added to the blocking buffer  
336 (0.1% Tween-20 / 10% filtered FCS in PBS) and embryos incubated overnight at 4°C.  
337 Embryos were then incubated for 3-4 hrs at room temperature with secondary antibodies in  
338 blocking buffer. All washes were done in filtered PBS + 0.05% Tween-20 (PBST). Pre-  
339 implantation embryos were permeabilized in 0.5% Triton X-100 in PBS for 20 min at room  
340 temperature. Primary antibodies were added in the blocking buffer (3% BSA in PBS + 0.1%  
341 Tween-20) and embryos incubated overnight at 4°C. For visualizing exocytotic vesicles  
342 through immunofluorescence permeabilization was performed with 0.1% (w/v) Saponin  
343 (Sigma S7900) + 0.2% (w/v) gelatin (Sigma G7765) + 5mg/ml BSA for 30 min at room  
344 temperature. Primary and secondary antibodies were prepared in 0.2% (w/v) gelatin + 0.01%  
345 (w/v) Saponin. Primary antibodies were added to the sample overnight at 4°C while  
346 secondaries were added for 2 hrs at room temperature after washing 3 times in PBS.

347 Primary antibodies used: ZO-1 (1:200; Thermofisher Scientific, 33-9100), E-cadherin (1:300;  
348 Thermofisher Scientific, 13-1900), aPKC (1:100; Santa Cruz Biotechnologies, sc-216), Oct4  
349 (1:400; Santa Cruz Biotechnologies, sc-5279), GM130 (1:200; BD, 610822), Laminin (1:400;  
350 Sigma, L9393), Cdx2 (1:200; Biogenex, MU392A-UC),  $\beta$ 1-integrin (1:50; Ha2/5; BD,  
351 561796), active  $\beta$ 1-integrin (1:50; 9EG7; BD, 553715), Ap2 $\gamma$  (1:300; Santa Cruz  
352 Biotechnologies, sc-8977), Eomes (1:400; Abcam, ab23345), Elf5 (1:400; Santa Cruz  
353 Biotechnologies, sc-9645), Podocalyxin (1:300; R&D systems, MAB1556), Pard6b (Santa  
354 Cruz Biotechnologies, sc-67393), pMLC (1:100; Cell Signalling Technologies, 3671P),  
355 Collagen IV (1:100; Millipore, AB769), HSPG2 (1:100; Millipore, MAB1948P), Rab11a  
356 (1:100; Cell Signalling Technologies, 2413S) Anxa2 (1:700; Abcam, ab41803). Secondary  
357 antibodies in pre-implantation blocking buffer were then added to the embryos for ~2 hrs at  
358 room temperature. Secondary antibodies used: Alexa 647 donkey anti-rabbit (1:500;  
359 Thermofisher Scientific, A31573), Alexa 594 donkey anti-rat (1:500; Thermofisher

360 Scientific, A21209), Alexa 568 donkey anti-mouse (1:500; Thermofisher Scientific,  
361 A10037), Alexa 488 donkey anti-mouse (1:500; Thermofisher Scientific, A21202), Alexa  
362 488 donkey anti-goat (1:500; Thermofisher Scientific, A11055), Phalloidin 488 (1:500;  
363 Thermofisher Scientific, A12379). All washes were done in PBS + 0.1% Tween-20. Nuclear  
364 staining: minimum 15 min incubation in DAPI + PBS (5mg/ml).

365 **Imaging:** Freshly recovered and fixed embryos were imaged on a Leica SP5 or SP8 confocal  
366 microscope. For live imaging a multiphoton Leica SP8 was used. The wavelengths used for  
367 2-photon excitation fluorescence (2PEF) when imaging mTmG (unconverted; Tomato) and  
368 LifeAct (GFP) were 1040nm and 910nm respectively.

369 **Laser ablation** was carried out on two-photon microscope (LaVision BioTec TriM Scope II).  
370 A multiphoton Insight DeepSee dual-line laser tuned to 920 nm was used to perform  
371 ablations. A region of interest was set to cell-cell interface and scanned at 3 different Z  
372 planes (1µm) with the multiphoton laser set at 70% transmission with a pixel dwell time of  
373 9.1µs. Images were taken immediately before, after and every 1 min following ablation.

374 **Image processing and analysis:** Fiji image processing software was used while 3D  
375 reconstructions of cells were carried out on 3D Slicer software using manually segmented  
376 images from Fiji.

377 **Cell culture:** Unconverted Confetti TSCs derived in defined conditions on fibronectin were  
378 used for TSCs aggregate experiments. TSCs were maintained and passaged under defined  
379 conditions on fibronectin-coated wells as described previously<sup>32</sup>. The cells were passaged  
380 when they reached ~70% confluency (normally once every three days) and medium was  
381 changed the day after passaging and then every other day. The cells were kept at 37°C in 5%  
382 CO<sub>2</sub>.

383 **Trophoblast stem cell aggregates:** TSCs were incubated for 2 min at 37°C in 0.05% trypsin-  
384 EDTA (Invitrogen) when they reached confluency. Trypsinization was stopped by adding TS  
385 medium (RPMI 1640 (Sigma), 20% FCS (GIBCO), penicillin/streptomycin (50µm/ml)  
386 (GIBCO), Sodium pyruvate (1Mm) (GIBCO), β-mercaptoethanol (100µM), L-glutamine  
387 (2mM) (GIBCO)). The cell suspension was collected and spun down (1000 rpm for 5 min).  
388 The supernatant was discarded, and the pellet re-suspended as clumps in defined culture  
389 medium prior to plating in Matrigel (BD, 356230). Using a haemocytometer the cell density  
390 was worked out and then appropriate volume of cell suspension was aspirated to suspend  
391 ~20000 cells/Matrigel drop. The cell suspension was spun down (1000 rpm for 5 min) and

392 supernatant removed. The TSCs in the pellet were gently re-suspended as clumps in a volume  
393 of Matrigel corresponding to 20ul / drop before plating each 20ul drop in one well of an  
394 ibiTreat microscopy plastic  $\mu$  plate (Ibidi). After 2 min of incubation at 37°C to allow  
395 polymerization of the Matrigel, the media were added according to the designed experiment.  
396 For cells grown in the absence of Matrigel, cells were plated on a non-adherent suspension  
397 culture plate (CELLSTAR, 662 102). The cells were kept at 37°C in 5% CO<sub>2</sub>.

398 **Embryo laser capture microdissection and RNA isolation:** The spatial transcriptome of  
399 embryos was obtained according to the Geo-seq methods<sup>33</sup>. In brief, E5.25, E5.5, E5.75 MF1  
400 embryos in deciduas were embedded in OCT compound and cryo-sectioned serially at 15  $\mu$ m  
401 along the proximodistal embryo axis. Serial sections were mounted on polyethylene  
402 terephthalate-coated slides. Frozen sections were allowed to thaw at room temperature and  
403 then dehydrated in ice-cold 100% ethanol. Fixation was performed in 75% ethanol, then the  
404 slides were stained with 1% cresyl violet acetate solution (Sigma-Aldrich, prepared in 75%  
405 ethanol), dehydrated in a series of 75%, 95%, 100% ethanol (30 secs for each step), and  
406 finally subjected to LCM on an MMI Cellcut Plus system (MMI, Zurich, Switzerland).

407 Approximately 20 cells in each section were harvested by LCM. Cell samples were lysed in  
408 50  $\mu$ l of 4 M guanidine isothiocyanate solution (GuSCN; Invitrogen, 15577-018) at 42°C for  
409 10 min. The volume of the lysate was adjusted to 200  $\mu$ l by nuclease-free water, and was  
410 further concentrated by ethanol precipitation in the presence of 1/10 volume of acetate  
411 sodium (pH 5.7, 3 M; Ambion) and 2  $\mu$ l of carrier glycogen (20 mg/ml; Roche). Total RNA  
412 pellets were dissolved in lysis solution and used as a template for low-cell number RNA-seq.

413 **RNA-Seq data pre-processing:** Raw reads were evaluated the quality with the FASTQC.  
414 Density distribution of gene expression for all samples were also plotted to assess whether  
415 there are inconsistent samples. Raw reads were mapped to mm10 version of mouse genome  
416 using Tophat2 v2.0.4 program<sup>34</sup>. We calculated fragment per kilobase per million (FPKM) as  
417 expression level using Cufflinks v2.0.2 with default parameters<sup>35</sup>. Genes with the FPKM >  
418 1.0 in at least one sample across all samples were retained for further analysis. Finally, the  
419 expression levels were transformed to logarithmic space by using the  $\log_2(\text{FPKM}+1)$ .

420 **Hierarchical clustering and PCA** are based on all the expressed genes as described in the  
421 RNA-Seq data pre-processing.

422 **Differentially expressed genes (DEGs) analysis** between epiblast (EPI) and extra-  
423 embryonic ectoderm (ExE) were identified using RankProd<sup>36</sup> with P value < 0.05 and fold  
424 change > 1.5.

425 **Functional enrichment analysis** of gene sets with different expression patterns was  
426 performed using the Database for Annotation, Visualization and Integrated Discovery v6.8  
427 (DAVID v6.8)<sup>37</sup>.

428 **Gene expression visualization:** to visualize the genes expression patterns in each embryo  
429 section, we wrote a program for visualization in MATLAB (version: 2015a). To analyze the  
430 genes expression dynamics during development (E5.25, E5.5, E5.75), we normalized the  
431 three sequencing batches to the same standard using ComBat<sup>38</sup>, then ran the MATLAB  
432 program.

### 433 **Statistics and Reproducibility**

434 Statistical analyses were performed using GraphPad Prism 6.0 software. Embryos were  
435 randomly allocated to control and experimental groups. Sample size was determined based  
436 on previous experimental experience. Investigators were not blinded to group allocation.  
437 Quantitative data are presented as mean ± s.e.m. Quantitative data were analysed using a  
438 two-sided unpaired Student's *t*-test and qualitative data were analysed with  $\chi^2$  test. Unless  
439 otherwise noted, each experiment was performed at least three times

### 440 **Data availability:**

441 RNA-seq data that support the findings of this study have been deposited in the Gene  
442 Expression Omnibus (GEO) under accession code GSE110808. Source data for Fig. 1b,  
443 2c,2e,2g,2i,2j,2l,3c,3h and Supplementary Fig. 3c,3d have been provided as Supplementary  
444 Table 2. Source data for Fig. 1g,h; Fig 3e,f; Fig. 4d,f; Fig. 5c,d and Fig. S3c are provided as  
445 supplementary movies. All other data supporting the findings of this study are available from  
446 the corresponding author on reasonable request.

### 447 **References**

- 448 1 Ang, S. L. & Constam, D. B. A gene network establishing polarity in the early mouse embryo.  
449 *Semin Cell Dev Biol* **15**, 555-561, (2004).
- 450 2 Kojima, Y., Tam, O. H. & Tam, P. P. Timing of developmental events in the early mouse  
451 embryo. *Semin Cell Dev Biol* **34**, 65-75, (2014).
- 452 3 Arnold, S. J. & Robertson, E. J. Making a commitment: cell lineage allocation and axis  
453 patterning in the early mouse embryo. *Nat Rev Mol Cell Biol* **10**, 91-103, (2009).

454 4 Rossant, J. & Tam, P. P. New Insights into Early Human Development: Lessons for Stem Cell  
455 Derivation and Differentiation. *Cell Stem Cell* **20**, 18-28, (2017).

456 5 Bedzhov, I. & Zernicka-Goetz, M. Self-organizing properties of mouse pluripotent cells  
457 initiate morphogenesis upon implantation. *Cell* **156**, 1032-1044, (2014).

458 6 Shahbazi, M. N. *et al.* Pluripotent state transitions coordinate morphogenesis in mouse and  
459 human embryos. *Nature* **552**, 239-243, (2017).

460 7 Lee, J. L. & Streuli, C. H. Integrins and epithelial cell polarity. *J Cell Sci* **127**, 3217-3225, (2014).

461 8 Barczyk, M., Carracedo, S. & Gullberg, D. Integrins. *Cell Tissue Res* **339**, 269-280, (2010).

462 9 Hiramatsu, R. *et al.* External mechanical cues trigger the establishment of the anterior-  
463 posterior axis in early mouse embryos. *Dev Cell* **27**, 131-144, (2013).

464 10 Shih, H. P., Panlasigui, D., Cirulli, V. & Sander, M. ECM Signalling Regulates Collective Cellular  
465 Dynamics to Control Pancreas Branching Morphogenesis. *Cell Rep* **14**, 169-179, (2016).

466 11 Stephens, L. E. *et al.* Deletion of beta 1 integrins in mice results in inner cell mass failure and  
467 peri-implantation lethality. *Genes Dev* **9**, 1883-1895 (1995).

468 12 Sakai, T., Larsen, M. & Yamada, K. M. Fibronectin requirement in branching morphogenesis.  
469 *Nature* **423**, 876-881, (2003).

470 13 Blankenship, J. T., Backovic, S. T., Sanny, J. S., Weitz, O. & Zallen, J. A. Multicellular rosette  
471 formation links planar cell polarity to tissue morphogenesis. *Dev Cell* **11**, 459-470, (2006).

472 14 Trichas, G. *et al.* Multi-cellular rosettes in the mouse visceral endoderm facilitate the  
473 ordered migration of anterior visceral endoderm cells. *PLoS Biol* **10**, e1001256, (2012).

474 15 Harding, M. J., McGraw, H. F. & Nechiporuk, A. The roles and regulation of multicellular  
475 rosette structures during morphogenesis. *Development* **141**, 2549-2558, (2014).

476 16 Bryant, D. M. *et al.* A molecular network for de novo generation of the apical surface and  
477 lumen. *Nat Cell Biol* **12**, 1035-1045, (2010).

478 17 Riedl, J. *et al.* Lifeact mice for studying F-actin dynamics. *Nat Methods* **7**, 168-169, (2010).

479 18 Muzumdar, M. D., Tasic, B., Miyamichi, K., Li, L. & Luo, L. A global double-fluorescent Cre  
480 reporter mouse. *Genesis* **45**, 593-605, (2007).

481 19 Peng, G. *et al.* Spatial Transcriptome for the Molecular Annotation of Lineage Fates and Cell  
482 Identity in Mid-gastrula Mouse Embryo. *Dev Cell* **36**, 681-697, (2016).

483 20 Rivera-Perez, J. A. & Magnuson, T. Primitive streak formation in mice is preceded by  
484 localized activation of Brachyury and Wnt3. *Dev Biol* **288**, 363-371, (2005).

485 21 Jung, J. J. *et al.* Syntaxin 16 regulates lumen formation during epithelial morphogenesis. *PLoS*  
486 *One* **8**, e61857, (2013).

487 22 Willenborg, C. *et al.* Interaction between FIP5 and SNX18 regulates epithelial lumen  
488 formation. *J Cell Biol* **195**, 71-86, (2011).

489 23 Mrozowska, P. S. & Fukuda, M. Regulation of podocalyxin trafficking by Rab small GTPases in  
490 2D and 3D epithelial cell cultures. *J Cell Biol* **213**, 355-369, doi:10.1083/jcb.201512024  
491 (2016).

492 24 Takeda, T., Go, W. Y., Orlando, R. A. & Farquhar, M. G. Expression of podocalyxin inhibits  
493 cell-cell adhesion and modifies junctional properties in Madin-Darby canine kidney cells. *Mol*  
494 *Biol Cell* **11**, 3219-3232 (2000).

495 25 Hoijman, E., Rubbini, D., Colombelli, J. & Alsina, B. Mitotic cell rounding and epithelial  
496 thinning regulate lumen growth and shape. *Nat Commun* **6**, 7355, (2015).

497 26 Kesavan, G. *et al.* Cdc42-mediated tubulogenesis controls cell specification. *Cell* **139**, 791-  
498 801, (2009).

499 27 Portereiko, M. F. & Mango, S. E. Early morphogenesis of the *Caenorhabditis elegans*  
500 pharynx. *Dev Biol* **233**, 482-494, (2001).



501 28 Villasenor, A., Chong, D. C., Henkemeyer, M. & Cleaver, O. Epithelial dynamics of pancreatic  
502 branching morphogenesis. *Development* **137**, 4295-4305, (2010).

503 29 Yang, Z. *et al.* De novo lumen formation and elongation in the developing nephron: a central  
504 role for afadin in apical polarity. *Development* **140**, 1774-1784, (2013).

505 30 Kao, R. M., Vasilyev, A., Miyawaki, A., Drummond, I. A. & McMahon, A. P. Invasion of distal  
506 nephron precursors associates with tubular interconnection during nephrogenesis. *J Am Soc  
507 Nephrol* **23**, 1682-1690, (2012).

508 31 Bedzhov, I., Leung, C. Y., Bialecka, M. & Zernicka-Goetz, M. In vitro culture of mouse  
509 blastocysts beyond the implantation stages. *Nat Protoc* **9**, 2732-2739, (2014).

510 32 Ohinata, Y. & Tsukiyama, T. Establishment of trophoblast stem cells under defined culture  
511 conditions in mice. *PLoS One* **9**, e107308, (2014).

512 33 Chen, J. *et al.* Spatial transcriptomic analysis of cryosectioned tissue samples with Geo-seq.  
513 *Nat Protoc* **12**, 566-580, doi:10.1038/nprot.2017.003 (2017).

514 34 Trapnell, C., Pachter, L. & Salzberg, S. L. TopHat: discovering splice junctions with RNA-Seq.  
515 *Bioinformatics* **25**, 1105-1111,(2009).

516 35 Kim, D. *et al.* TopHat2: accurate alignment of transcriptomes in the presence of insertions,  
517 deletions and gene fusions. *Genome biology* **14**, R36, doi:10.1186/gb-2013-14-4-r36 (2013).

518 36 Hong, F. *et al.* RankProd: a bioconductor package for detecting differentially expressed  
519 genes in meta-analysis. *Bioinformatics (Oxford, England)* **22**, 2825-2827, 6 (2006).

520 37 Huang da, W., Sherman, B. T. & Lempicki, R. A. Systematic and integrative analysis of large  
521 gene lists using DAVID bioinformatics resources. *Nature protocols* **4**, 44-57, (2009).

522 38 Johnson, W. E., Li, C. & Rabinovic, A. Adjusting batch effects in microarray expression data  
523 using empirical Bayes methods. *Biostatistics (Oxford, England)* **8**, 118-127, (2007).

524

## 525 **Figure legends**

### 526 **Figure 1: Stages of embryo remodeling and pro-amniotic cavity formation**

527 (a) Morphological staging of early post-implantation embryos based on the development of a  
528 pro-amniotic cavity; Arrowhead points to apical side of extra-embryonic ectoderm (ExE)  
529 cells at the boundary and arrows point to the ExE cells facing the epiblast (EPI) cavity;  
530 circled portion of stage III embryo highlights the invading EPI cavity into the ExE. n=142  
531 embryos. (b) Quantification of the distance between the EPI and ExE cavities during pro-  
532 amniotic cavity formation. Two sided unpaired student's t-test; \*\*\*\*P<0.0001; mean±SEM;  
533 n= 21 stage II, 28 stage III and 20 stage IV embryos. (c) Percentages of embryos found in  
534 specific pro-amniotic cavity stages according to embryonic day staging systemn; =73 E5.5 +  
535 31 E5.75 embryos.(d) Schematic representation of the five major stages of pro-amniotic  
536 cavity formation as identified through analysis of freshly recovered embryos. VE, visceral  
537 endoderm; ECM, extracellular matrix; EPC, ectoplacental cone. (e) Magnification of the area  
538 at the EPI-ExE boundary from d showing the reorientation of EPI boundary cells (red  
539 arrows). (f) Extra-embryonic cavity formation. Each stage of extra-embryonic cavity (cyan

540 asterisks) formation was characterized by localization of tight junction protein ZO-1 (white  
541 arrowheads) and enrichment of E-cadherin (yellow arrowheads) as well as cell shape changes  
542 accompanied with bending of the tissue (white arrows). Yellow asterisk indicates embryonic  
543 cavity. White dots mark ExE proximal cells acquiring columnar morphology. Red dots: cell  
544 apical site; P: proximal; D: distal. n=25 embryos. (g) Stills from a time-lapse movie showing  
545 apical constriction driven tissue bending during extra-embryonic cavity formation. Red  
546 arrowheads mark apical actin enrichment during apical cell constriction which leads to cell  
547 ingression and tissue bending. Dotted line: cavity. Segmented panel: Red outline marks cells  
548 undergoing apical constriction. Yellow line: tissue outline. Note that these cells ingress  
549 inducing tissue bending and cavity formation. Green outline: lateral cells. n=5 embryos. (h)  
550 Stills from single cells in (g); Cells show apical surface area reduction before ingression.  
551 Enrichment of apical actin (red arrowheads) coincides with apical constriction. Scale  
552 bars=20um.

553 **Figure 2: Extra-cellular matrix/ $\beta$ 1-integrin signalling is essential for extra-embryonic**  
554 **ectoderm polarization and morphogenesis**

555 (a) Polarity pattern assessment in stage II E5.5 extra-embryonic ectoderm (ExE) based on  
556 Golgi position(GM130); Schematic: position of Golgi in manually segmented and position-  
557 based colour coded ExE. White dots: Golgi. n=10 embryos. (b) Cell morphology of outside  
558 (i) and inside (i') cells as shown by 3D cell segmentation. (c) Cell aspect ratio of outside vs  
559 inside ExE cells. Two sided unpaired student's t-test; \*\*\*\*P<0.0001;mean $\pm$  SEM; n=50  
560 cells, 6 E5.5 embryos. (d) TSCs grown as aggregates in Matrigel for 48 hrs in the presence of  
561 N2B27 and FGF2, stained for tight junction marker ZO-1 or golgi marker GM130, F-actin  
562 and the TSC marker Eomes. n=3 biological replicates. (e) Cell aspect ratio of outside (n=31)  
563 vs inside cells(n=36) in TSCs .Two sided unpaired student's t-test; \*\*\*\*P<0.0001;  
564 mean $\pm$ SEM. (f) Cell morphology of outside ExE cells in control and COLIV treated  
565 embryos. Embryos in each group are shown at two different z slices and a zoomed image of  
566 outside cells is displayed on right of each image. n=3 biological replicates. (g) Comparison of  
567 cell aspect ratio of outside cells in control and COLIV-treated embryos. Long axis = axis  
568 perpendicular to basement membrane; short axis = axis perpendicular to long axis at half  
569 length; Two sided unpaired student's t-test; \*\*\*\*P<0.0001; mean $\pm$ SEM; n=60 cells, 6  
570 Control and 10 COLIV treated embryos. (h) TSC aggregates cultured in Matrigel in the  
571 presence of N2B27 and FGF2 for 48 hrs.  $\beta$ 1-integrin function blocking antibody (Ha2/5) was  
572 added at 24hrs. n=3 biological replicates. (i) Quantification of apical ZO-1 subcellular

573 localization (apical ZO-1 intensity/basolateral ZO-1 intensity) in control (n=40 cells) and  $\beta$ 1-  
574 integrin function-blocking antibody-treated TSC aggregates (n=40 cells); Two sided unpaired  
575 student's t-test; \*\*\*\*P<0.0001; mean $\pm$ SEM. (j) Comparison of cell aspect ratio of outside  
576 cells in control (n=51 cells) and  $\beta$ 1-integrin function-blocking antibody-treated TSC  
577 aggregates (n=32 cells) Two sided unpaired student's t-test; \*\*\*\*P<0.0001; mean $\pm$ SEM. (k)  
578 Basement membrane disruption after treatment with COLIV leads to failure of pro-amniotic  
579 cavity formation. (l) Quantification of pro-amniotic cavity formation efficiency in control and  
580 COLIV-treated embryos;  $\chi^2$  test ; \*\*\*\*P<0.0001. For (k) and (l) n= 27 control and 24  
581 COLIV-treated embryos. n=3 biological replicates. Scale bars=20um.

582 **Figure 3: Extracellular matrix-dependent 3D rosette formation throughout the extra-**  
583 **embryonic ectoderm**

584 (a) Representative examples of E5.5 embryos showing formation of extra-embryonic  
585 ectoderm (ExE) rosettes as identified by cell morphology. n=20 embryos. (b) E5.5 embryos  
586 stained to reveal tight junctions (ZO-1), polarity (aPKC, Par6) and actomyosin markers (F-  
587 actin, pMLC). Magnified images centered on ExE rosettes (outlined by dashed line). Arrows:  
588 rosette center. n=20 embryos. (c) Average number of ExE rosettes observed per stage of pro-  
589 amniotic cavity development (17 stage II, 21 stage III, 23 stage IV, 10 stage V embryos; Two  
590 sided unpaired student's t-test; \*\*\*P=0.0002; mean $\pm$ SEM. (d) Representative image of an  
591 E5.5, stage III embryo. Orthogonal projections are displayed on the right and bottom of the  
592 image. Asterisks label bipolar cells in the rosette either having a second apical side in the  
593 ExE cavity or the epiblast cavity. Rosette schematics are displayed on the bottom right with  
594 red dots indicating bipolar cells. Inset shows magnified image of the rosette. n=10 embryos.  
595 (e) Rosettes identified and segmented at different z optical sections from a single E5.5, stage  
596 III embryo. Segmented panel: Segmented cells for each rosette are differentially and  
597 arbitrarily colour-coded for 3D rotation clarity. 3D Rendering panel: Each cell is also coded  
598 with a roman numeral (rosette 1: i – vi; rosette 2: i' – vi'). Rotation and magnification of  
599 rosette centres indicated by the dashed circle demonstrate absence of self-contained lumen as  
600 apical surface of cells meet at rosette centre. (f) Combined 3D rendered rosettes in the same  
601 spatial frame to assess cell sharing. Shared cells are highlighted. Both colour and number  
602 coding is retained from (e) and displayed in this panel. Magnification of rosette centres  
603 indicated on top right of each box. (g) ExE rosette formation in control and COLIV treated  
604 embryos. Orthogonal slices are projected on the right and bottom of the images. n=12  
605 embryos;3 biological replicates. (h) Percentage of embryos with or without identified ExE

606 rosettes in control and COL IV-treated groups.  $\chi^2$  test ; \*\*\*\*P<0.000; n= 12 control and 12  
607 COLIV treated embryos; 3 biological replicates. (i) Model of ECM/ $\beta$ 1-integrin-mediated  
608 signalling mechanism for polarity establishment and rosette formation in ExE. Scale  
609 bars=20um.

610

611

612 **Figure 4: Epiblast-extra-embryonic ectoderm hybrid rosette polarized resolution drives**  
613 **epiblast reorganization**

614 (a) Two representative examples of hybrid rosette forming at the EPI (filled dots)/extra-  
615 embryonic ectoderm (ExE) (hollow dots) boundary. Arrowhead: pMLC enrichment. Insets  
616 show EPI/ExE boundary. Dashed lines in magnified images indicate ExE cells where solid  
617 lines indicate EPI cells. Dashed outline in example II points to an ExE rosette. YZ orthoslice  
618 is projected on the right of example II. n=10 embryos. (b) Peri- and early post-implantation  
619 embryos stained for laminin to assess integrity of basement membrane between EPI and polar  
620 trophoderm (pTE)/ExE (yellow arrowheads). White dots indicate pTE cells. n=15  
621 embryos. (c) Freshly recovered embryos at different stages of hybrid rosette development.  
622 Rosette resolution is displayed in a temporal sequence from left to right. solid outlines: EPI  
623 cells; dashed outlines: ExE cells; grey outline: EPI cavity. Arrow: pMLC puncta belonging to  
624 the resolved rosette. Inset in right panel shows a different Z slice where the re-oriented EPI is  
625 evident. n= 8 embryos. (d) Stills from a time-lapse movie of LifeAct-GFP E5.5 (late Stage II)  
626 embryo showing EPI/ExE hybrid rosette resolution and EPI reorganisation. Green box  
627 magnifications indicate the centre of hybrid rosette, made up of EPI ( blue dots) and ExE  
628 cells (red dots) as it loses the actin enrichment (yellow arrowheads) in preparation for  
629 resolution. Green box at 80min time-point highlights an ExE rosette in proximity to EPI  
630 cavity. Red dots indicate rosette cells. Right panel: Manually segmented version of the time-  
631 lapse movie focusing on the resolving hybrid rosette and a forming EPI cavity proximal  
632 rosette (green in second row).n= 3 embryos. (e) Representative E5.5 embryo with EPI/ExE  
633 hybrid rosette formed at the EPI/ExE boundary. Arrowhead: rosette centre; Arrows: Polarized  
634 tract; Hollow dots: ExE cells; Filled dots: EPI cells. n=6 embryos. (f) Left panel: Still images  
635 from time lapse movie after laser ablation of adhesion sites connecting the EPI cavity with  
636 hybrid rosette centre. Red line: ablation site. Right panel: Magnified images of the boundary  
637 region before and after ablation. Purple region with green outline shows the EPI cavity.

638 Arrows show the ablated adhesion site and the progression of the cavity after ablation. n=2  
639 biological replicates. Scale bars=20um.

640 **Figure 5: Rosette formation/resolution-mediated pro-amniotic cavity formation**

641 (a) Representative example of stage III E5.5 embryo. Magnified images show extra-  
642 embryonic ectoderm (ExE) rosette in proximity to epiblast (EPI) cavity with segmented  
643 counterparts. Arrows point to polarized tracts (assessed with tight junction marker ZO-1)  
644 extending from EPI cavity to centre of rosette before EPI cavity progression. n=10 embryos.  
645 (b) Representative examples (I & II) of stage IV E5.5 embryos. Magnified images show  
646 resolved ExE rosette in proximity to EPI cavity with segmented counterparts. Arrows point to  
647 expanded apical domain (assessed with polarity marker aPKC) of ExE cells after rosette  
648 resolution and EPI cavity progression. Asterisks indicate cells which lost their connection  
649 upon rosette resolution. n=10 embryos. (c) Left panel: Stills from a time-lapse movie of  
650 mTmG stage III embryo transitioning to stage IV of pro-amniotic cavity development. Box  
651 (i) focuses on the EPI-ExE boundary and segmentation analysis is shown in middle panel.  
652 Cells are manually segmented and differentially and arbitrarily colour-coded for clarity.  
653 Extraction of segmented-only data is displayed next in right panel for the period of 40–  
654 100min where formation and resolution of rosette is observed. Arrows in right panel indicate  
655 rosette resolution and EPI cavity progression. n= 3 embryos. (d) Stills from a time-lapse  
656 movie of Lifeact-GFP embryo showing ExE cavity extension through polarized rosette  
657 resolution. Note the loss of actin enrichment from polarized tract (arrows) connecting the  
658 cavity with the rosette centre (arrowhead) before rosette resolution. Yellow filled area; ExE  
659 cavity; Magenta dots: rosette cells; Green dots; cells that lost adhesion; n=3 embryos. Scale  
660 bars=20um.

661 **Figure 6: Spatial transcriptome analysis of pro-amniotic cavity formation**

662 (a) Experimental strategy: cells were captured by laser capture microdissection along the  
663 proximodistal embryo axis and analysed by RNA-seq (Methods). Purple: epiblast (EPI);  
664 Cyan: extra-embryonic ectoderm (ExE); Yellow: VE. P: proximal; D: distal. (b) Differential  
665 gene expression analysis heat maps for gene ontology terms: exocytosis, vesicle organization.  
666 E5.25: sections 2-4 EPI, sections 6-8 ExE; E5.5: sections 2,4,5 EPI, sections 6-11 ExE; E5.75  
667 sections 3-8 EPI, sections 10-19 ExE. Purple outlines highlight genes previously reported to  
668 be involved in lumen formation. (c) Expression pattern of selected genes during post-  
669 implantation development. Left: Schematic showing the position and tissue identity for each

670 sequenced section (numbers on the left of the plot) in E5.25, E5.5 and E5.75 embryos. Gene  
671 expression is presented as colour coded corn plot. Colour coding represents  $\log_2$  (FPKM+1)  
672 values. FPKM: fragment per kilobase per million.

673

674

675

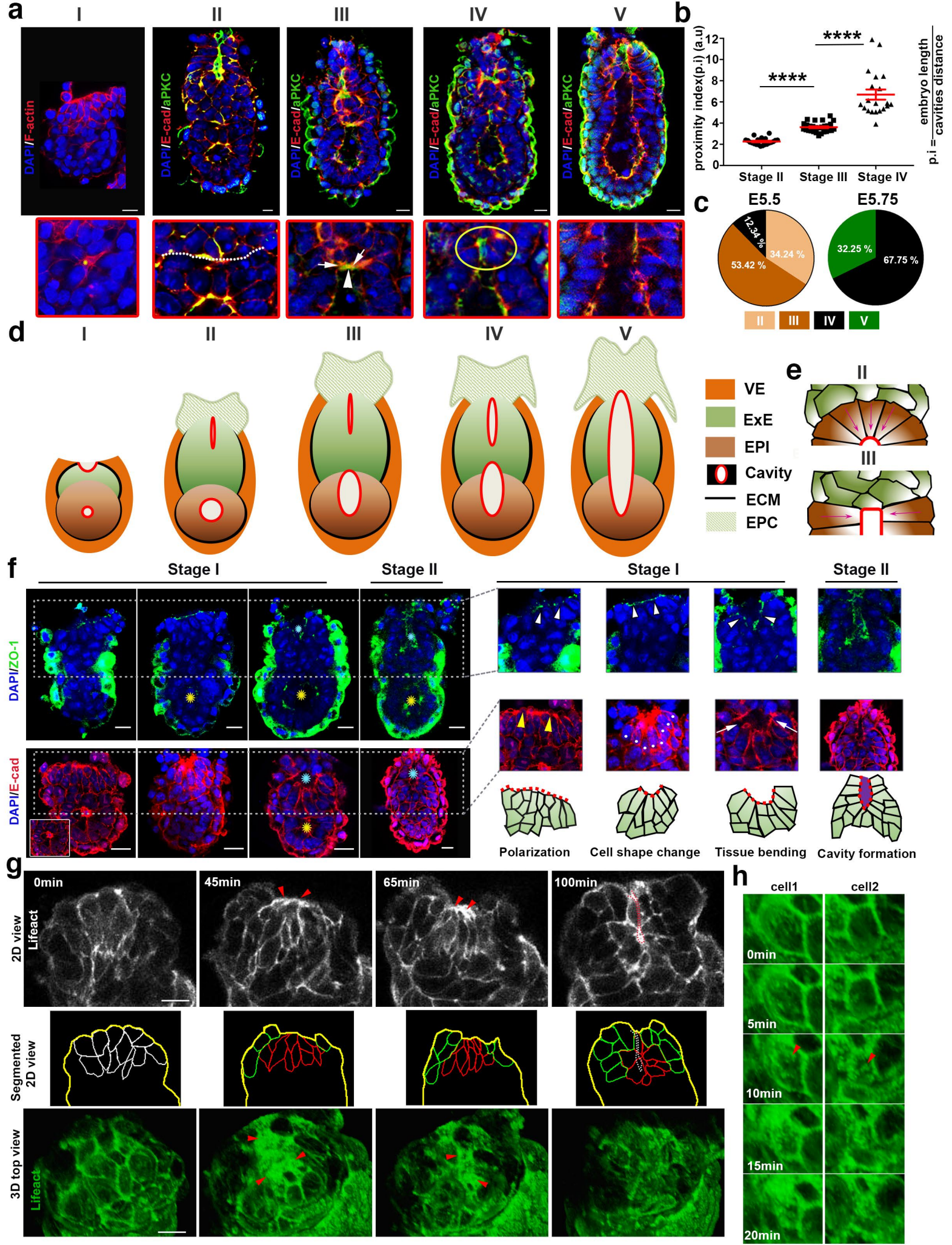
676 **Figure 7: Polarized pattern of Podocalyxin exocytosis during rosette resolution and**  
677 **cavities expansion**

678 (a) Annexin A2 localization in a representative E5.5 embryo. n=10 embryos. (b)  
679 Rab11/Podocalyxin localization in E5.5 embryo. Arrows show Rab11/Podocalyxin positive  
680 exocytotic vesicles. n=10 embryos. (c) Representative E5.5 embryo with epiblast (EPI)/extra-  
681 embryonic ectoderm (ExE) hybrid rosette (dots). Lower panel shows magnified images of  
682 EPI/ExE boundary. Arrow indicated the polarized tract connecting the EPI cavity with the  
683 rosette centre. Arrowheads show Rab11 and Podocalyxin positive vesicles docking cell/cell  
684 interfaces forming the polarized tract. n=5 embryos. (d) Representative Z-stacks of an E5.5  
685 embryo. Upper panel shows an ExE rosette being connected with the EPI cavity via polarized  
686 tract (arrows). Rab11/Podocalyxin positive vesicles are docked (hollow arrowhead) or  
687 polarized along the polarized tract (filled arrowhead). Lower panel shows ExE rosette being  
688 connected with the ExE cavity via polarized tract (arrows). Rab11/Podocalyxin positive  
689 vesicles are docked along the polarized tract (hollow arrowhead). n=5 embryos. (e) Maximum  
690 intensity profile image of a representative E5.75 embryo just after cavities fusion. A unified  
691 cavity (arrows) spans the embryonic and extra-embryonic compartment. Exocytotic vesicles  
692 are present in extra-embryonic cells not directly in contact with the cavity (arrowheads). n=5  
693 embryos Scale bars=20um.

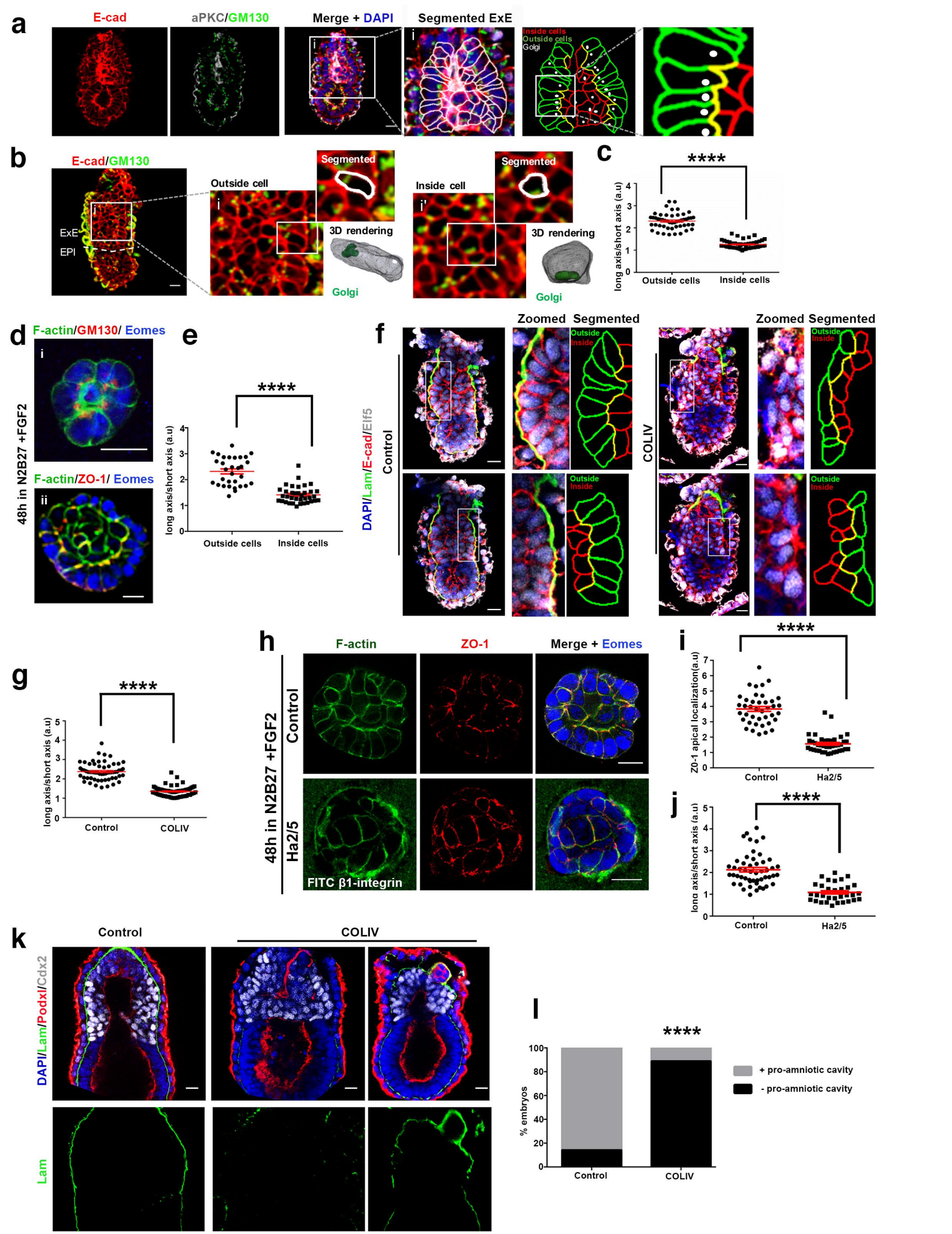
694 **Figure 8: Cell intercalation during the final step of pro-amniotic cavity formation**

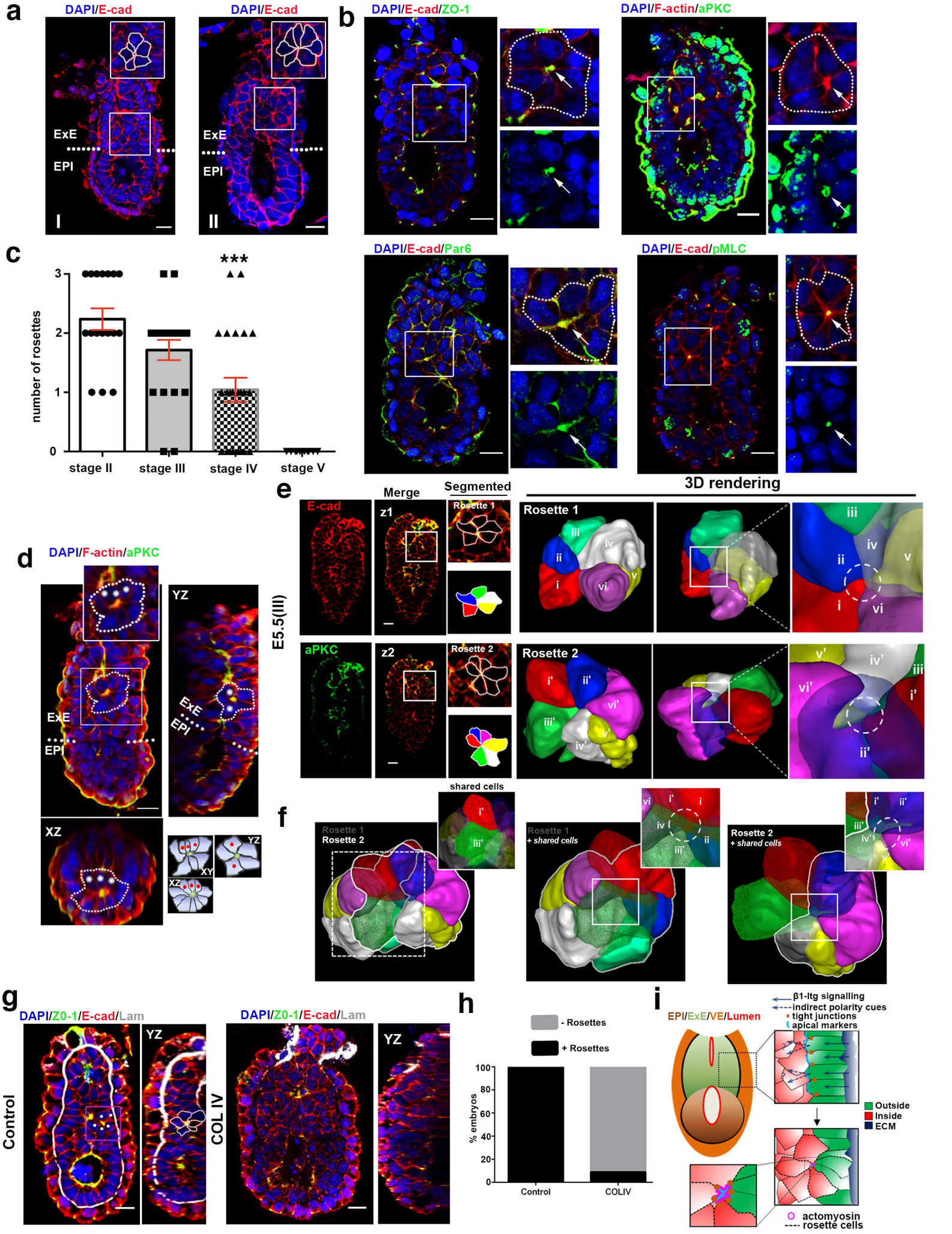
695 (a) Time-lapse movie extraction of an mTmG E5.5 (stage II) embryo with segmented cavities  
696 (purple) showing a cell (green) intercalating towards the basement membrane. n=2 embryos.  
697 (b) Representative example of an E6.25 embryo. At this stage all ExE cells contribute to the  
698 unified pro-amniotic cavity and ExE is a pseudostratified epithelium. All ExE cells are  
699 negative for intracellular exocytotic vesicles. n=10 embryos. (c) Model of pro-amniotic cavity  
700 formation. During stage I, the epiblast cavity forms through hollowing and the polar  
701 trophoctoderm proliferates to form the extra-embryonic ectoderm (ExE). The ExE cells

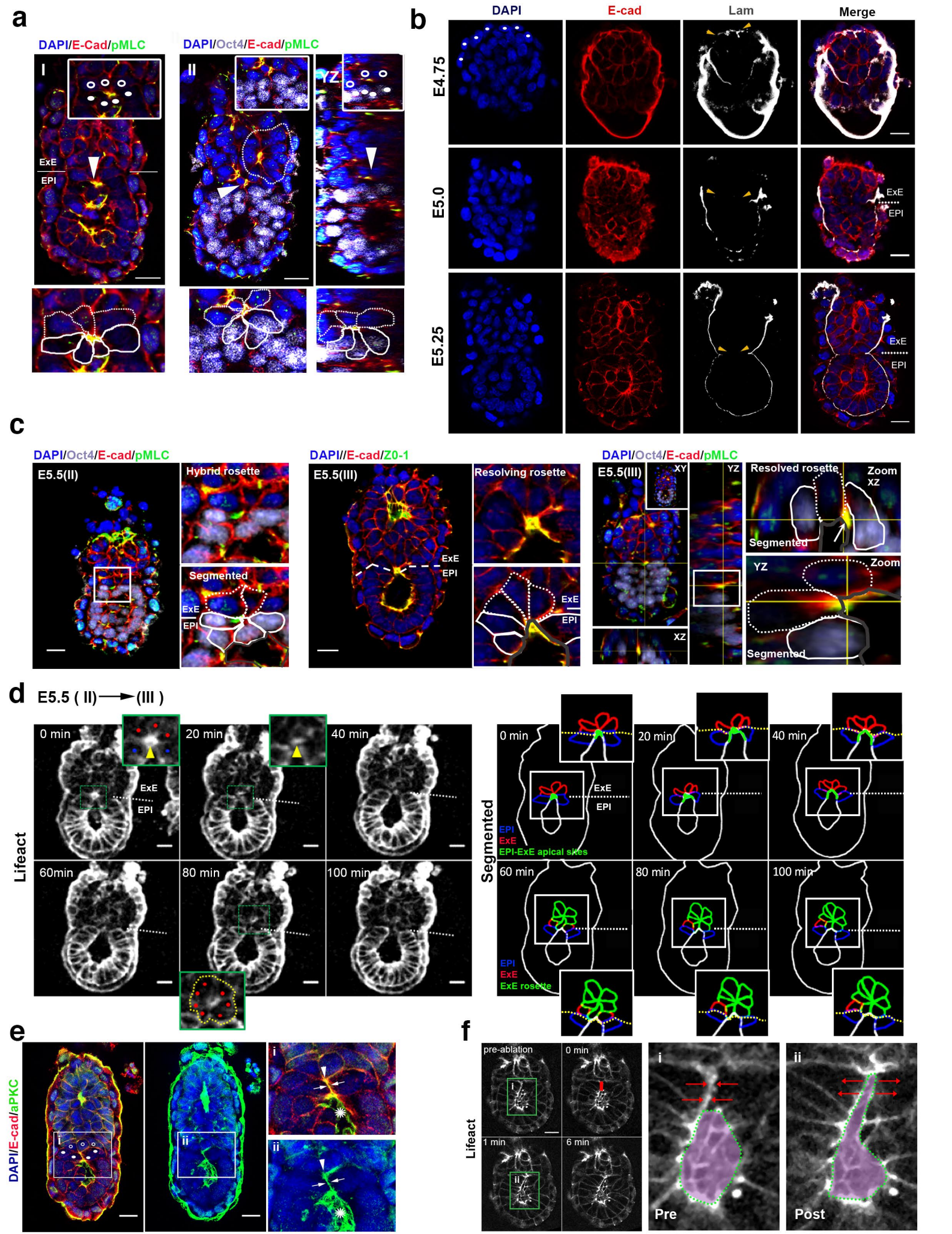
702 undergo apical constriction, which induces the formation of the ExE cavity through tissue  
703 folding. At stage II, in the presence of embryonic and ExE cavities, a hybrid rosette forms at  
704 the embryonic/extra-embryonic boundary. Polarized resolution of this rosette results in  
705 remodeling of embryonic compartment and progression to stage III. After, extra-embryonic  
706 rosettes form and undergo polarized resolution, the embryonic and extra-embryonic cavities  
707 extend. At stage IV the extended cavities merge. At stage V, a newly-formed unified pro-  
708 amniotic cavity spans the egg cylinder. Scale bars=20um.

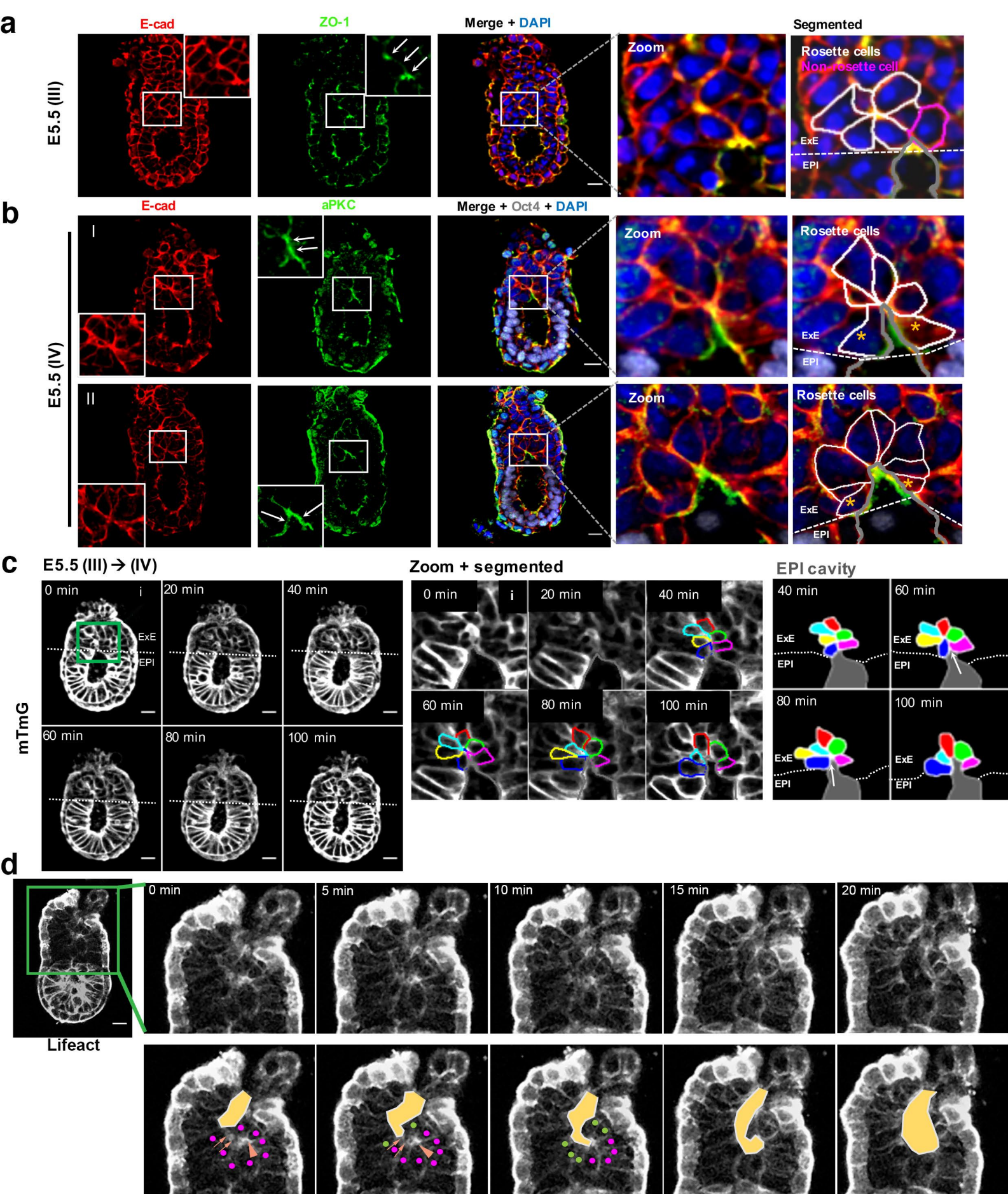


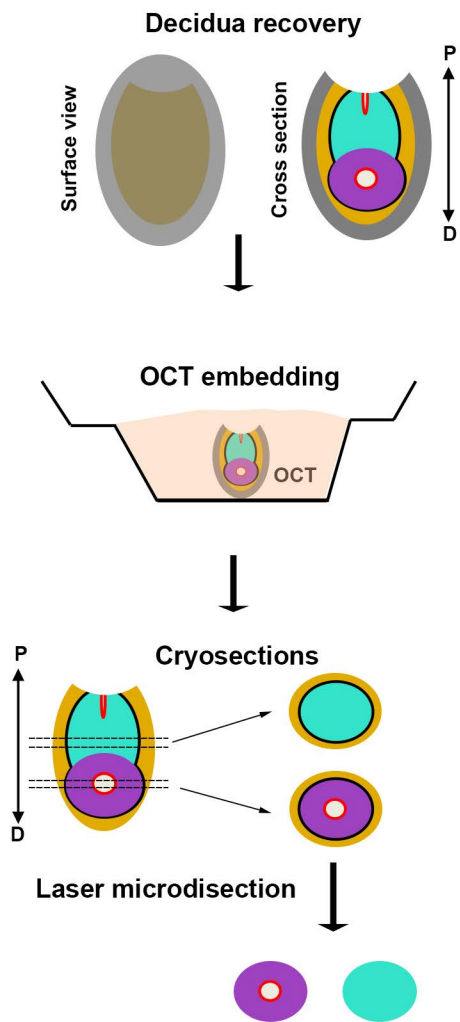
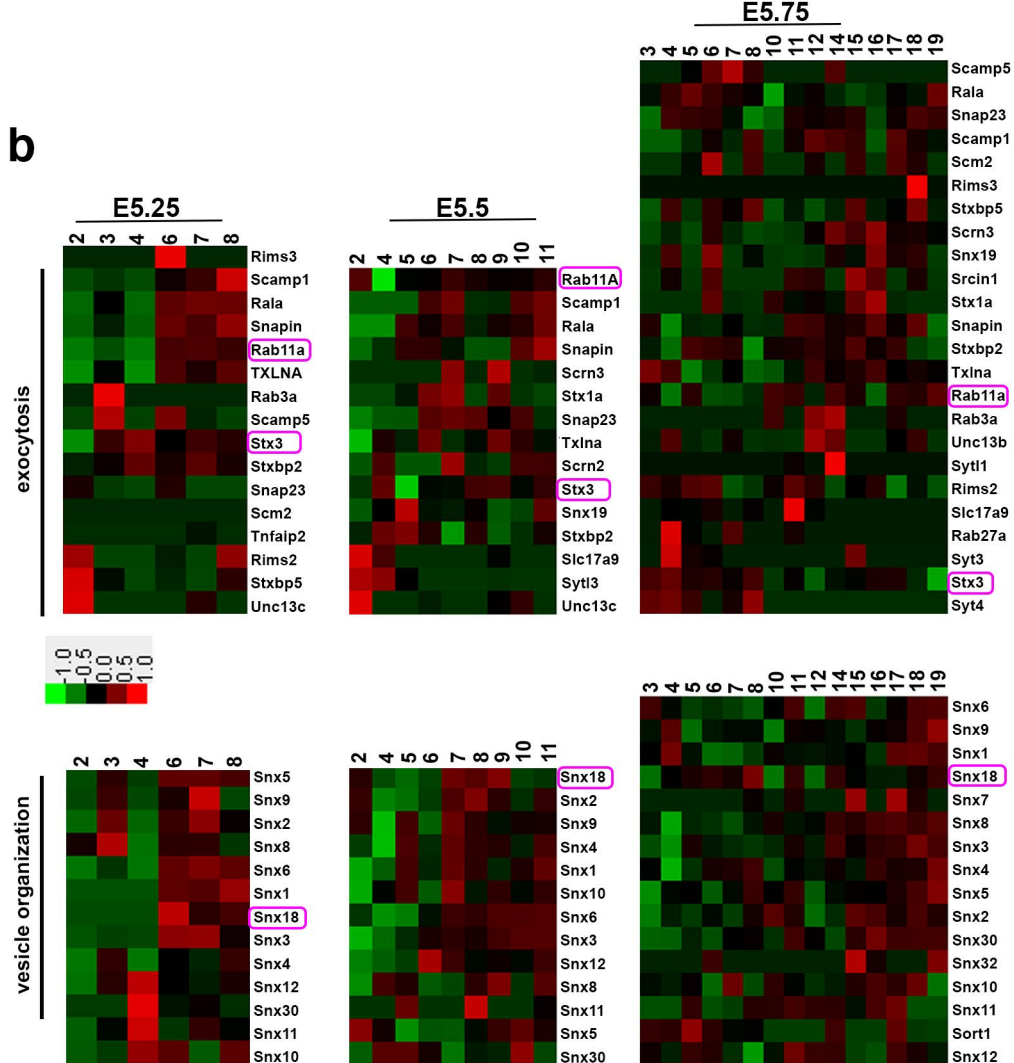










**a****b****c**